Chemical Science

ROYAL SOCIETY OF CHEMISTRY

EDGE ARTICLE

View Article Online
View Journal | View Issue

Cite this: *Chem. Sci.*, 2024, **15**, 14778

All publication charges for this article have been paid for by the Royal Society of Chemistry

Customizing dumbbell-shaped heterostructured artificial photosystems steering versatile photoredox catalysis†

Peng Su,[a] Xian Yan[a] and Fang-Xing Xiao *[ab]

Benefiting from their excellent light-capturing ability, suitable energy band structure and abundant active sites, transition metal chalcogenides (TMCs) have been attracting widespread attention in heterogeneous photocatalysis. Nonetheless, TMCs still suffer from sluggish charge transfer kinetics, a rapid charge recombination rate and poor stability, rendering the construction of high-performance artificial photosystems challenging. Here, a ternary dumbbell-shaped CdS/MoS_2/CuS heterostructure with spatially separated catalytically active sites has been elaborately designed. In such a heterostructured nanoarchitecture, MoS_2 clusters, selectively grown on both ends of the CdS nanowires (NWs), act as terminal electron collectors, while CuS nanolayers, coated on the sidewalls of CdS NWs through ion exchange, form a P–N heterojunction with the CdS NW framework, which accelerates the migration of holes from CdS to CuS, effectively suppressing the oxidation of sulfide ions and improving the stability of CdS NWs. The well-defined dumbbell-shaped CdS/MoS_2/CuS ternary heterostructure provides a structural basis for spatially precise regulation of the charge migration pathway, where photogenerated electrons and holes directionally migrate to the MoS_2 and CuS catalytic sites, respectively, ultimately achieving efficient carrier separation and significantly enhancing photoactivity for both photocatalytic hydrogen generation and selective organic transformation under visible light. Moreover, we have also ascertained that such ion exchange and interface configuration engineering strategies are universal. Our work features a simple yet efficient strategy for smartly designing multi-component heterostructures to precisely modulate spatially vectorial charge separation at the nanoscale for solar-to-hydrogen conversion.

Received 21st July 2024
Accepted 14th August 2024

DOI: 10.1039/d4sc04838e

rsc.li/chemical-science

1. Introduction

With the rapid increase in global energy demand, energy and environmental issues have become increasingly prominent, driving the rapid development of sustainable clean energy.[1–3] The advantages of solar energy, including abundance, sustainability and environmental friendliness, render solar-driven photocatalysis a viable solution to the aforementioned challenges.[4,5] In the past few decades, photocatalysis technology has been thrivingly developed including photocatalytic hydrogen production, CO_2 reduction and nitrogen fixation, selective organic transformation, and environmental remediation.[6–8] However, its development is retarded by the confined light absorption scope, poor photostability, and high electron–hole recombination rate of semiconductor materials, reducing the solar energy conversion efficiency and posing significant challenges in constructing robust and sustainable artificial photocatalytic systems.[9–11]

Among the diverse semiconductor materials, transition metal chalcogenides (TMCs) have been widely explored due to their suitable energy band structure, outstanding light-capturing ability and enriched active sites.[12,13] However, widespread applications of TMCs in heterogeneous photocatalysis are still hindered by sluggish charge transfer kinetics, severe photo-corrosion and a rapid charge recombination rate. To solve these problems, multifarious strategies have thus been proposed to optimize the photocatalytic efficiency of TMC photosystems, such as metal or non-metal element doping, co-catalyst loading and heterojunction engineering.[14–16] Among them, co-catalyst modification represents a simple and feasible method for constructing high-efficiency TMC photocatalytic systems by providing abundant surface catalytically active sites and reducing the activation energy of surface redox reactions.[17–20] Nevertheless, it should be emphasized that the interfacial integration mode between TMCs and co-catalysts is of paramount importance for the effective separation of photogenerated charge carriers, which is heavily dependent on

[a]College of Materials Science and Engineering, Fuzhou University, New Campus, Minhou, Fujian Province, 350108, China

[b]State Key Laboratory of Structural Chemistry, Fujian Institute of Research on the Structure of Matter, Chinese Academy of Sciences, Fuzhou, Fujian 350002, P. R. China. E-mail: fxxiao@fzu.edu.cn

† Electronic supplementary information (ESI) available. See DOI: https://doi.org/10.1039/d4sc04838e

applicable interface engineering techniques, aimed at meticulously constructing directional charge transfer pathways.

Constructing TMC heterostructure photosystems *via* exquisite, easily accessible, and tunable interface configuration regulation provides a feasible and efficient approach to enhance the photoactivities by maximizing the synergy of ingredients for enhanced interfacial charge transport and separation. In such a well-designed nanoarchitecture, favorable energy level alignment among the building blocks, decent interface integration fashion, and increased active sites concurrently enhance the carrier transport kinetics, prolong the carrier lifetime, and enhance the stability of heterostructure photosystems.[21–23] Apart from heterojunction engineering, spatially precise co-catalyst loading on heterostructure photocatalysts provides an additional efficacious route to further strategically mediate charge migration by remarkably reducing the activation energy, providing charge trapping sites, and reinforcing charge flow impetus. Inspired by the structural merits of one-dimensional (1D) TMCs, which feature spatially unidirectional high-efficiency charge transport along the 1D framework, we believe that selectively positioning appropriate co-catalysts at both ends and sidewalls of 1D TMCs for designing a dumbbell-shaped composite photocatalyst is beneficial for engendering spatially separated vectorial charge migration channels. In this way, carrier migration pathways over the customized dumbbell-shaped heterostructure can be precisely modulated, which significantly diminishes the charge accumulation and enhances the charge separation.

In this work, a ternary dumbbell-shaped CdS/MoS_2/CuS heterostructure photosystem was designed *via* progressive interface modulation. Specifically, as a proof-of-concept investigation, CdS nanowires (NWs) are selected as a quintessential TMC substrate, and then a dumbbell-shaped CdS/MoS_2 binary nanocomposite was prepared by selectively growing MoS_2 clusters at both ends of CdS NWs through a hydrothermal reaction. Subsequently, CuS was uniformly coated on the sidewall of CdS NWs through a facile ion exchange strategy. The thus-formed P–N heterojunction at the contact interface between CdS and CuS promotes electron transfer from CuS to CdS, while holes migrate from CdS to CuS under the driving force of the built-in electric field, avoiding the accumulation of holes. At the same time, MoS_2 clusters at both ends of CdS provide abundant reactive sites to quickly trap the electrons for photoreduction catalysis including photocatalytic hydrogen generation and photoreduction of aromatic nitro compounds to amino derivatives under visible light. The synergistic effect of MoS_2 and CuS concomitantly promotes the charge separation/migration of the CdS/MoS_2/CuS ternary heterostructure. Our work conceptually demonstrates the smart design of robust, stable and well-defined heterostructure photocatalysts with spatially separated charge transport pathways for solar energy conversion.

2. Experimental section

2.1. Preparation of CdS nanowires (NWs)

CdS NWs were fabricated *via* a hydrothermal method. The detailed synthesis procedures are provided in the ESI.†

2.2. Preparation of the CdS/MoS_2 nanodumbbell binary nanocomposite

CdS/MoS_2 nanodumbbells were prepared by a hydrothermal method using CdS NWs as the substrate. The detailed information on the synthesis procedures is provided in the ESI.†

2.3. Preparation of CdS/MoS_2/CuS nanodumbbell ternary nanocomposites

CdS/MoS_2/CuS nanodumbbell heterostructures were synthesized through a cation exchange strategy using CdS/MoS_2 (CM^2) nanodumbbells as the precursor. Specifically, 100 mg of CM^2 nanodumbbell catalyst was dispersed in 100 mL deionized water under ultrasonic treatment. Then, a certain amount of $CuCl_2 \cdot 2H_2O$ aqueous solution (0.1 M) was added to the above suspension and vigorously stirred for 1 h. The samples were precipitated, centrifuged, washed and dried overnight at 60 °C. The loading percentage of CuS was controlled by adjusting the volume of $CuCl_2 \cdot 2H_2O$ aqueous solution, and samples incorporating 0.2 mL, 0.4 mL, 1.2 mL, 2 mL, and 3.2 mL of 0.1 M $CuCl_2 \cdot 2H_2O$ aqueous solution were designated as $CM^2Cu^{0.5}$, CM^2C^1, CM^2C^3, CM^2C^5, and CM^2C^8, respectively.

2.4. Characterization

The crystal phase was explored by X-ray diffraction (XRD, X'Pert Pro MPD, Philips, Holland). Morphologies were probed by field emission scanning electron microscopy (FESEM, Supra55, Carl Zeiss, Germany). Transmission electron microscopy (TEM) images were recorded using a TEM microscope system (JEOL-2010). X-ray photoelectron spectroscopy (XPS) spectra were collected on a photoelectron spectrometer (ESCALAB 250, Thermo Scientific, America), for which the binding energy (B.E.) of all tested elements was calibrated using the B.E. of C 1s (284.80 eV). Fourier transform infrared (FTIR) spectra were collected using an infrared spectrophotometer (TJ270-30A, Tianjin, China). Raman spectra were studied using a Raman spectrometer (Dxr-2xi, Thermo Scientific, America). Ultraviolet-visible (UV-vis) light diffuse reflectance spectroscopy (DRS) was performed on a UV-vis spectrophotometer (Cary 7000, Varian, America), for which the reflectance background is $BaSO_4$ ranging from 200 nm to 800 nm. Photoluminescence (PL) spectra were recorded on a Varian Cary Eclipse spectrometer.

2.5. Photocatalytic hydrogen evolution

Photocatalytic hydrogen evolution measurements were conducted using a 300 W Xe lamp (PLSSXE300D, Beijing Perfect Light Co. Ltd, China) equipped with an optical cutoff filter ($\lambda >$ 420 nm) as the light source. Specifically, 10 mg of the catalyst was dispersed in 5 mL Na_2S/Na_2SO_3 ($Na_2S : Na_2SO_3 = 0.25$ mol : 0.35 mol) solution and stirred throughout the reaction. Photocatalytic activities were evaluated based on the H_2 evolution amount in the first 2 h of the reaction. The H_2 amount was analyzed on an online gas chromatograph (Shimadzu GC-8A). Cyclic photocatalytic H_2 evolution measurements were carried out as follows: the photocatalytic reaction system was thoroughly degassed after the first run reaction without separating

the photocatalysts or supplementing Na_2S/Na_2SO_3 and, subsequently, the thoroughly degassed reaction system was irradiated again under the same conditions.

The apparent quantum yield (A.Q.Y) of the reaction was defined by the following equation:

$$\text{A.Q.Y}(100\%) = \frac{\text{number of reacted electrons}}{\text{number of incident photons}} \times 100\% = \frac{\text{number of evolved hydrogen molecules} \times 2}{\text{number of incident photons}} \times 100\% \quad (1)$$

2.6. Photocatalytic reduction performances

In a typical photoreduction reaction, a 300 W Xe lamp (PLS-SXE300D, Beijing Perfect Light Co. Ltd, China) equipped with a 420 nm cut-off filter ($\lambda > 420$ nm) was used as the irradiation source. 10 mg of catalyst and 40 mg of ammonium formate (NH_4HCO_2) were added to 30 mL of nitroaromatics aqueous solution (20 ppm), which was saturated with N_2 bubbling under ambient conditions. Before visible light illumination, the above suspension was stirred in the dark for 1 h to ensure the establishment of adsorption–desorption equilibrium between the sample and reactant. During the process of the reaction, 2 mL of sample solution was collected at a certain time interval and centrifuged to remove the catalyst completely at 12 000 rpm and the supernatant was analyzed using a UV-vis absorption spectrophotometer (Thermal Genesis). Photoreduction of other aromatic nitro compounds was also carried out under identical conditions. The photoactivities of the samples are defined by the following formula.

$$\text{Conversion}\% = \frac{C_0 - C}{C_0} \times 100\% \quad (2)$$

where C_0 represents the initial concentration of nitroaromatics and C is the concentration after visible light irradiation for a certain time.

2.7. PEC measurements

PEC water oxidation measurements were carried out on an electrochemical workstation (CHI 660E, CHI Shanghai, Inc.) using a standard three-electrode configuration and 0.5 M Na_2SO_4 (pH = 7) aqueous solution as the electrolyte. Pure CdS NWs, CM^2 and CM^2C^1 (1 × 1 cm) were used as the working electrodes, and Pt foil and an Ag/AgCl (KCl) electrode served as the counter electrode and reference electrode, respectively. A 300 W Xe lamp (FX300, Beijing Perfect Light Co. Ltd, China) equipped with a UV-cutoff filter for visible light ($\lambda > 420$ nm) was applied as the light source for visible light irradiation. The potentials of the electrodes are corrected against the reversible hydrogen electrode (RHE) *via* the calibration equation as shown below:

$$E_{RHE} = E_{Ag/AgCl} + 0.059\text{pH} + E^{\circ}_{Ag/AgCl} \quad (3)$$

$$(E^{\circ}_{Ag/AgCl} = 0.1976 \text{ V at } 25\ ^{\circ}\text{C})$$

3. Results and discussion

3.1. Characterization of heterostructures

Scheme 1 illustrates the preparation process of a dumbbell-shaped CdS/MoS_2/CuS ternary heterostructure. CdS NWs were first prepared by a hydrothermal method using ethylenediamine as a chelating agent. Due to the increased surface energy, there is a difference in reactivity between the tip and the rod body of CdS NWs, and the selectivity of the tip is higher than that of the rod body, leading to preferential axial growth. Subsequently, a secondary hydrothermal reaction was carried out to introduce a molybdenum source, and MoS_2 clusters were grown at both ends to prepare the dumbbell-shaped CdS/MoS_2 binary nanocomposite. The MoS_2 clusters at both ends of CdS NWs serve as electron-capturing sites, promoting charge transfer along the axial direction of CdS NWs and accelerating carrier separation. Finally, considering that CuS (6.3×10^{-36})[24] has a smaller Ksp value than CdS (8.0×10^{-27}),[25] and the MoS_2 clusters at both ends of CdS are insoluble in water, Cu^{2+} ions can be used to replace the Cd^{2+} of CdS through a ion exchange strategy, forming a well-defined CdS/CuS P–N heterostructure on the CdS sidewall of binary dumbbell-shaped CdS/MoS_2 nanomaterials. The MoS_2 clusters at both ends are not replaced by Cu^{2+} ions but rather remain as hydrogen evolution active sites. It should be stressed that the internal electric field formed on the sidewall of the CdS in the heterostructure promotes the hole migration from CdS to CuS, enhancing the stability of the CdS NW substrate. The innovative design of such a ternary dumbbell-shaped CdS/MoS_2/CuS heterostructure ensures the spatial separation of reduction and oxidation sites, thereby significantly reducing the charge recombination rate and enhancing the photoactivity.

The morphology evolution of the catalyst was probed by field emission scanning electron microscopy (FESEM) measurements. Fig. 1a shows the FESEM image of CdS, which demonstrates a typical rod-shaped structure with a relatively smooth surface, and the diameter of the nanowires is about 30–50 nm. Fig. 1b shows the morphology of the CM^2 binary composite, from which it is apparent that MoS_2 clusters selectively grow at both ends of the CdS NWs, forming a dumbbell-like structure. Subsequently, a ternary dumbbell shaped CM^2C^1 heterostructure was constructed by cation exchange (replacing Cd^{2+} with Cu^{2+} ions) on the CdS sidewall of the dumbbell-shaped CdS/MoS2 binary composite. As displayed in Fig. 1c, it is evident that replacement of Cd^{2+} with Cu^{2+} ions does not inflict damage on the MoS_2 clusters situated at both ends, and the CM^2C^1 heterostructure still maintains the dumbbell-shaped structure. The structural characteristics of CM^2C^1 were further confirmed by transmission electron microscopy (TEM). Fig. 1d indicates that MoS_2 at both ends demonstrates a clear cluster structure. The microstructure and morphology of the dumbbell-shaped CM^2C^1 ternary heterostructure were further analyzed by HRTEM (Fig. 1e). From the locally enlarged HRTEM image (Fig. 1f and g), lattice fringes of 0.357 nm and 0.325 nm corresponding to the (100) and (110) crystal planes of CdS and CuS

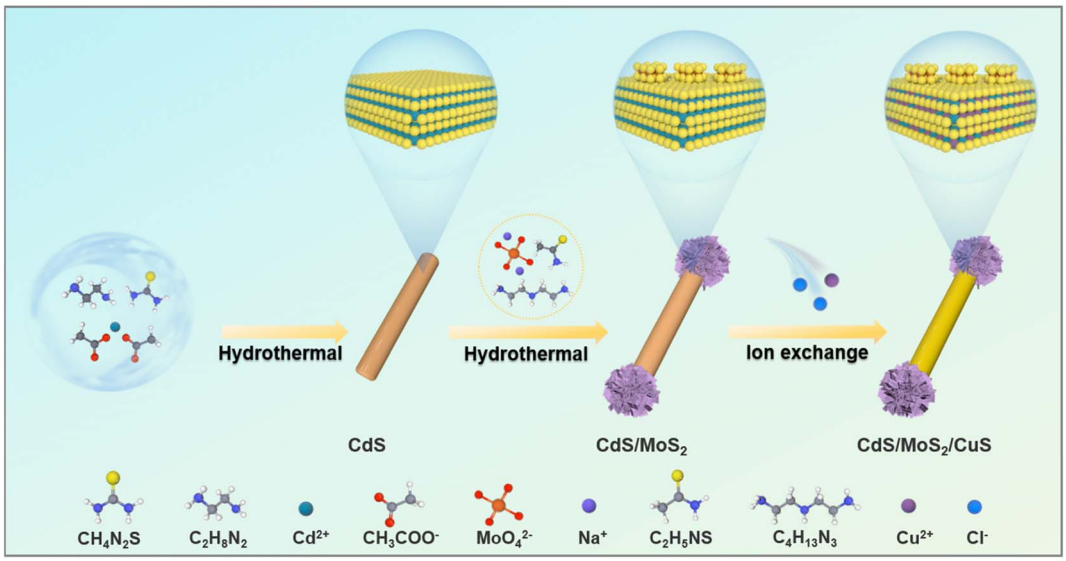

Scheme 1 Schematic illustration depicting the construction of the CdS/MoS_2/CuS nanodumbbell heterostructure.

are clearly observed.[26–28] To precisely determine the integration sites between CdS and CuS, TEM elemental mapping analysis was performed on CM^2C^1 (Fig. 1h–m). It was observed that Mo element was concentrated at the ends of the CdS NWs, further confirming the selective growth of MoS_2 clusters at the ends of the CdS NWs. Additionally, the distributions of Cu and Cd elements are consistent, both concentrating on the nanowire framework of CdS, indicating that CuS is accurately coated onto the CdS NWs through an ion exchange strategy. The above results indicate that a spatially controlled CdS/MoS_2/CuS ternary heterostructure has been successfully fabricated. The synergistic effect of MoS_2 clusters positioned at both ends and the ultrathin CuS layer coated on the CdS sidewalls provides a structural basis for the precise control of carrier transfer.

In addition to the intuitive morphology analysis, X-ray diffraction (XRD) is used to analyze the crystal structure of the sample. As shown in Fig. S1a,† pure CdS corresponds to a hexagonal phase (JCPDS No. 65-3414).[29] Only characteristic diffraction peaks of CdS are detected in the dumbbell-shaped CM^x ($x = 1, 2, 3, 4$) binary nanocomposite, and no characteristic diffraction peaks of MoS_2 are detected (Fig. S1b†), which is related to the low crystallinity (Fig. S1c†) and high dispersion of MoS_2. Moreover, it was revealed that the growth of MoS_2 at both ends of CdS NWs does not influence the crystal structure of CdS. Similarly, no characteristic peaks of MoS_2 and CuS are observed in the XRD pattern of the CM^2C^1 heterostructure, which is caused by the low content of CuS generated through cation exchange (Fig. 2a). Raman spectroscopy was employed to conduct further analysis on the structures of CdS, CM^2 and CM^2C^1 materials. As displayed in Fig. 2b, apparent vibrational peaks at 302 cm^{-1} and 605 cm^{-1} are observed, which are attributed to the 1 LO longitudinal optical and 2 LO phonon modes of hexagonal CdS,[26] respectively. It is worth noting that after selectively growing MoS_2 clusters at both ends of CdS NWs to construct dumbbell-shaped CM^2 composite materials, the Raman peaks of 1 LO and 2 LO show negative shifts. This is associated with the lattice strain induced by the selective growth of MoS_2 clusters at the ends of CdS NWs, where the bond length of the CdS lattice is stretched at the interface between CdS and MoS_2.[30] The Raman spectrum of the CM^2C^1 ternary heterostructure retains the 1 LO and 2 LO peaks of CdS, but these peaks are further negatively shifted compared with CM^2, which is related to the selective substitution of Cd^{2+} with Cu^{2+} ions on the sidewalls of CdS in the dumbbell-shaped CdS/MoS_2 binary composite. The above analysis confirms the successful construction of a dumbbell-shaped CM-Cu^1 heterostructure through the gradual introduction of MoS_2 and CuS. Fig. 2c shows the FTIR spectra of CdS, CM^2, and CM^2C^1, wherein the peak at 3435 cm^{-1} is attributed to the stretching vibration mode of the –NH group on the CdS surface.[31] The decreased peak intensity of CM^2 and CM^2C^1 at 3435 cm^{-1} indicates that the introduction of MoS_2 and CuS shields the –NH peak.[26,29] The optical properties of the samples were investigated by diffuse reflectance spectroscopy (DRS). As shown in Fig. 2d, the absorption band edge of pure CdS is approximately at 526 nm, which correlates with the photoexcitation of CdS. Compared with CdS, dumbbell-shaped CM^2 exhibits significantly enhanced light absorption in the visible light range, which is related to the selective growth of MoS_2 clusters at both ends of CdS NWs. The absorption capacity of the ternary dumbbell-shaped CM^2C^1 heterostructure in the visible light range is further enhanced, which can be attributed to the *in situ* formation of CuS with a narrower band gap on the sidewall of CdS, substantially boosting the light absorption capacity of the CM^2C^1 heterostructure. The loading of MoS_2 and CuS significantly enhances the light-capturing capability of CdS, laying the foundation for efficient photocatalytic reactions. As shown in Fig. 2e, the band gaps (E_g) of CdS, CM^2 and CM^2C^1 are determined to be 2.4, 2.37 and 2.34 eV, respectively, indicating that MoS_2 and CuS loading exerts limited influence on the E_g of CdS.

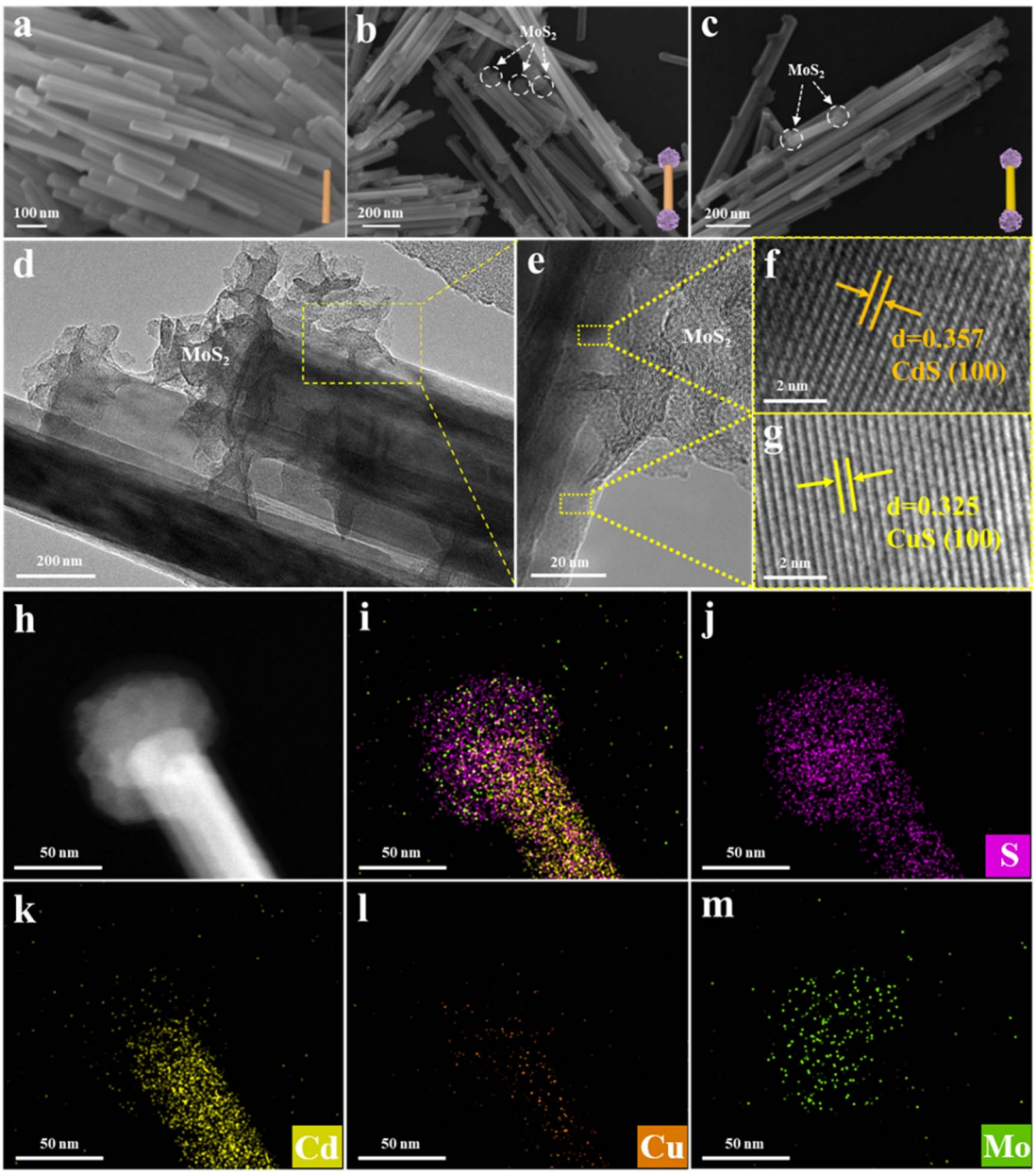

Fig. 1 SEM images of (a) CdS, (b) CM^2 and (c) CM^2C^1. (d) TEM and (e–g) HRTEM images of the CM^2C^1 nanodumbbell heterostructure, and elemental mapping results of (h–m) CM^2C^1.

The surface elemental composition and chemical state of the catalyst were analyzed by X-ray photoelectron spectroscopy (XPS). Fig. S2† shows the survey spectra of CdS and CM^2C^1 with the appearance of Cd, S, Mo and Cu signals in CM^2C^1, wherein Cd and S elements originate from CdS NWs, while Mo and Cu elements stem from MoS_2 and CuS, respectively. The high-resolution S 2p spectrum of pure CdS (Fig. 2fI) shows two peaks at 162.6 eV (S $2p_{1/2}$) and 161.37 eV (S $2p_{3/2}$) corresponding to the S^{2-} species,[29,30] respectively. As shown in Fig. 2gI, the peaks at 411.89 eV (Cd $3d_{3/2}$) and 405.16 eV (Cd $3d_{5/2}$) in the high-resolution Cd 3d spectrum of pure CdS correspond to the Cd^{2+} species,[32] respectively. Compared with CdS, the binding energies of S 2p (Fig. 2fII) in CM^2C^1 exhibit a red shift, indicating a strong electronic interaction between MoS_2 and CuS with CdS. Fig. 2h shows the high-resolution Cu 2p spectrum of CM^2C^1, wherein the peaks at 933.13 eV (Cu $2p_{3/2}$) and 953.07 eV (Cu $2p_{1/2}$) are attributed to the Cu^{2+} species.[33] The high-resolution Mo 3d spectrum of CM^2C^1 is shown in Fig. 2i, wherein the peaks at 229 eV (Mo $3d_{5/2}$) and 232.63 eV (Mo $3d_{3/2}$) correspond to the Mo^{4+} species of MoS_2, and the peaks at 235.88 eV (Mo $3d_{3/2}$) correspond to the Mo^{6+} species, which may be caused by Mo oxidation.[34,35] In addition, a peak at 225.87 eV corresponding to S 2s species is observed in the Mo 3d spectrum, which is associated with the Mo–S bonds of MoS_2.[36] The specific surface areas of CdS NWs, CM^2 and CM^2C^1 are determined to be approximately 14.47, 14.79, and 20.00 $m^2\ g^{-1}$, respectively (Fig. S3 and

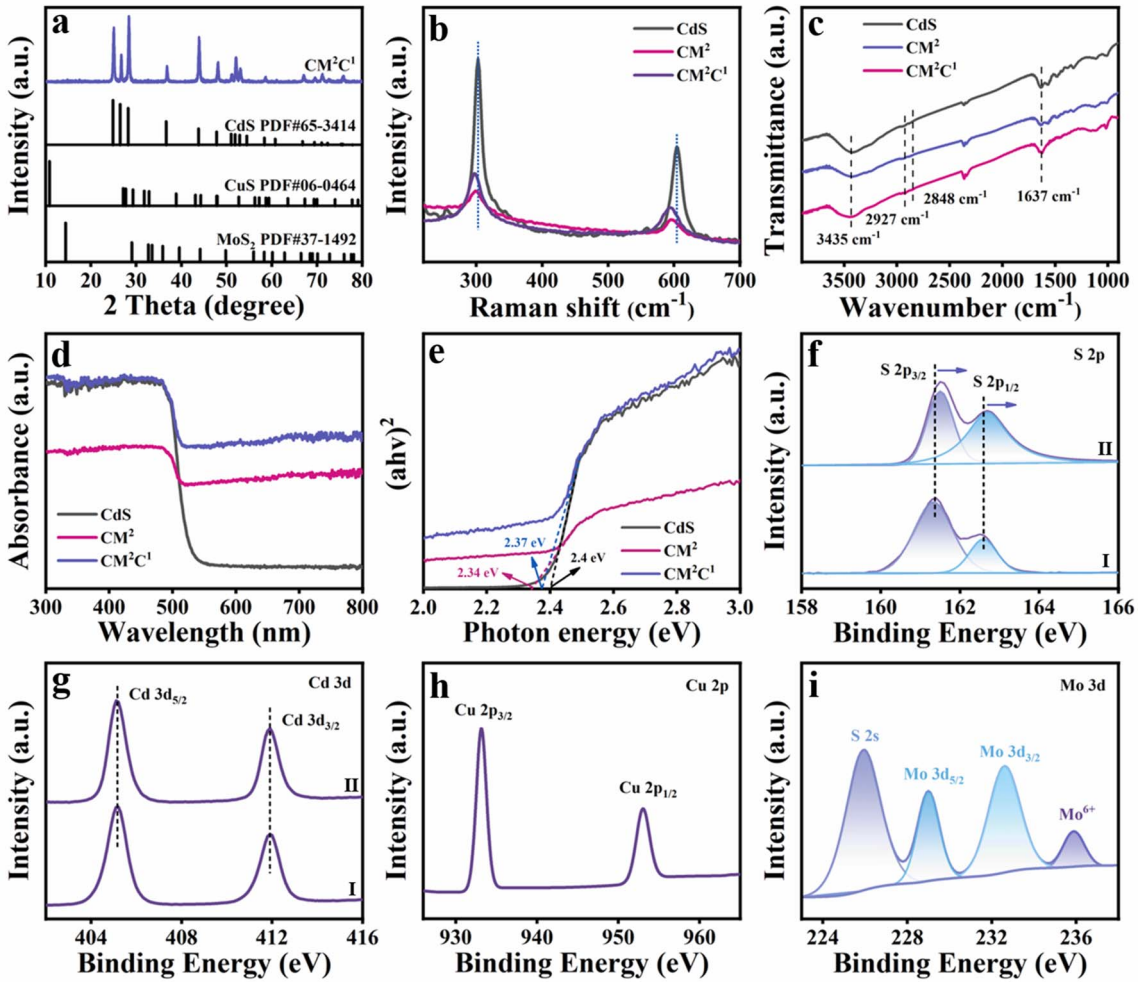

Fig. 2 (a) XRD patterns of the CM^2C^1 nanodumbbell heterostructure; (b) Raman, (c) FTIR, (d) DRS and (e) band-gap determination results of CdS, CM^2 and CM^2C^1; high-resolution (f) S 2p and (g) Cd 3d of (I) CdS and (II) CM^2C^1; high-resolution (h) Cu 2p and (i) Mo 3d of CM^2C^1.

Table S3†), indicating that the introduction of MoS_2 and CuS has no significant effect on the specific surface area of the nanocomposites.

3.2. Photocatalytic performances

The photocatalytic hydrogen generation performances of the samples were explored under visible light irradiation. As shown in Fig. 3a, pure CdS exhibits low photocatalytic hydrogen evolution activity due to severe photo-corrosion. Notably, its photoactivity is significantly enhanced after the introduction of MoS_2, with CM^2 displaying the highest hydrogen evolution activity, which is 16.7 times as high as that of pure CdS. We speculate that the MoS_2 clusters at both ends of CdS NWs serve as electron collectors, facilitating the charge migration from the CdS NWs to MoS_2 and then effectively reducing the recombination rate of charge carriers photoexcited over CdS. At the same time, the MoS_2 at both ends offers abundant reaction sites to further enhance the photocatalytic hydrogen evolution reaction, greatly improving the hydrogen evolution activity. With further adjustment of the amount of molybdenum source added, it was observed that the photocatalytic hydrogen evolution activity of CM^3 quickly decreases. This is due to the fact that introducing more MoS_2 inevitably forms carrier recombination centers on the surface of CdS NWs, which fails to effectively facilitate the directional migration of electrons along CdS NWs. This confirms the crucial role of selectively growing MoS_2 at both ends of CdS NWs in promoting charge transfer. The photoactivity of CM^4 is almost equivalent to that of pure CdS, indicating that the introduced amount of MoS_2 greatly exceeds the loading capacity of CdS, resulting in a shielding effect that is unfavorable for the participation of photoexcited electrons from CdS in the catalytic reaction. Fig. 3b shows the photocatalytic hydrogen evolution rate of the dumbbell-shaped CM^2C^x (x = 0.5, 1, 2, 3, 4) ternary heterostructures, among which CM^2C^1 exhibits the highest hydrogen evolution rate that is 3.4 times larger than that of CM^2. By selectively integrating MoS_2 and CuS onto CdS NWs, the synergistic effect of MoS_2 and CuS can be fully utilized, greatly enhancing the photocatalytic activity of the CM^2C^x photosystem. Meanwhile, to verify the superiority of selective loading of MoS_2 and CuS on CdS NWs, we prepared control samples of $CdS/CuS/MoS_2$ (C/C/M) and $CdS–CuS–MoS_2$ (C-C-M) ternary

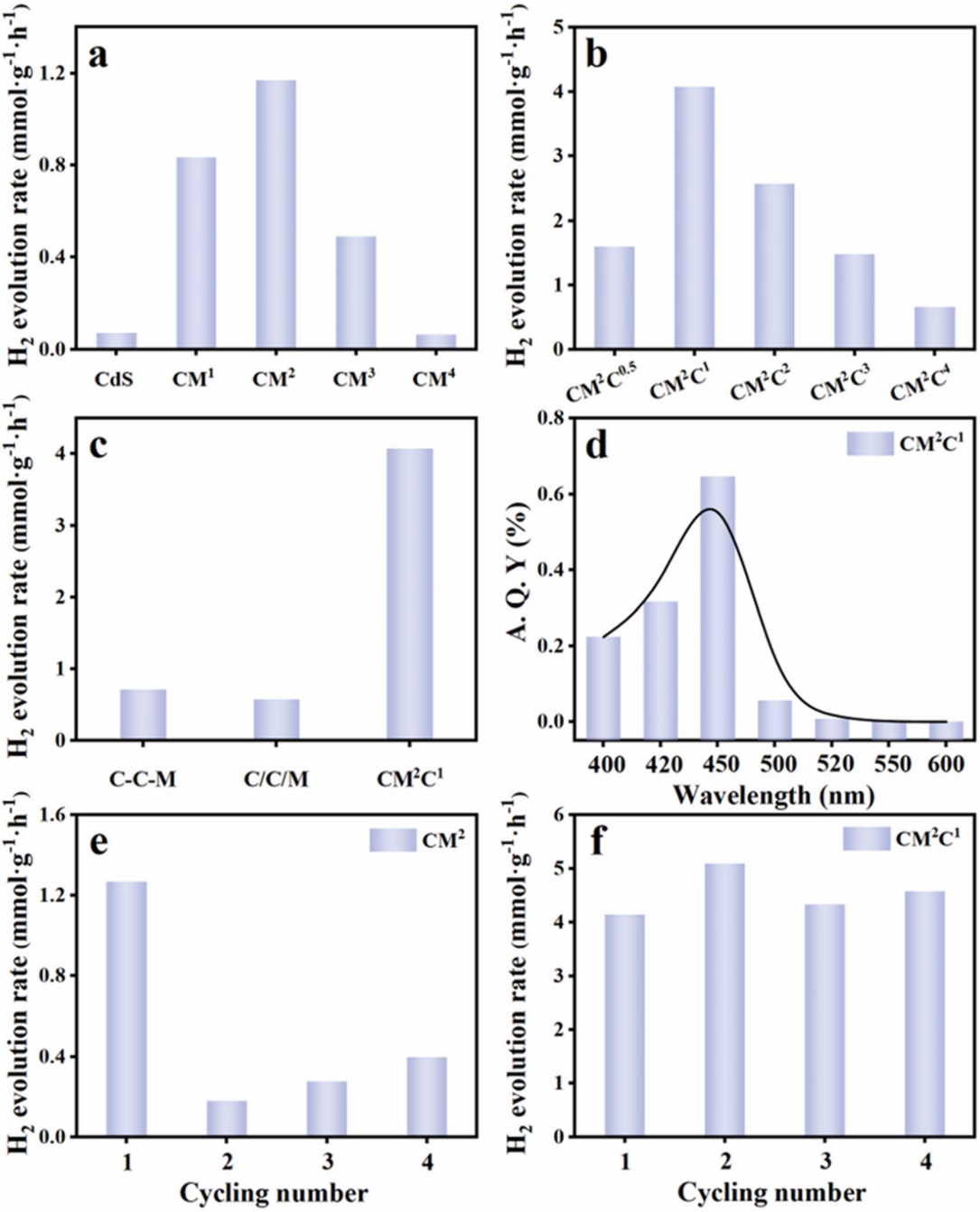

Fig. 3 Photocatalytic hydrogen evolution performances of (a) CdS and CM^x (x = 1, 2, 3, 4), and (b) CM^{2}C^x (x = 0.5, 1, 2, 3, 4). (c) Photocatalytic hydrogen evolution performances of C-C-M, C/C/M and CM^{2}C^1; (d) A.Q.Y result of CM^{2}C^1 under monochromatic light irradiation; photostability measurements of (e) CM^2 and (f) CM^{2}C^1.

nanocomposites and analyzed their photocatalytic hydrogen production performance (Fig. 3c). Through ion exchange, CuS is *in situ* generated on the surface of CdS, followed by the loading of an equal amount of MoS_2 to construct the C/C/M composite. In addition, during the *in situ* generation of CuS on the surface of CdS through the ion exchange strategy, an equal amount of MoS_2 was added, wherein MoS_2 and CuS are randomly loaded onto CdS NWs to construct the C-C-M composite. The photoelectron transfer models of CdS/MoS_2/CuS, C-C-M, and C/C/M heterostructures are shown in Fig. S4a–c.† CdS/MoS_2/CuS exhibits a unique dumbbell-shaped structure (Fig. S4a†), where MoS_2 clusters play an important role as electron collectors to withdraw the electrons from CdS, and simultaneously, CuS enables the formation of a p–n heterojunction with the CdS substrate to enhance hole transfer. Under the synergistic effect of MoS_2 clusters and CuS, photoinduced electrons and holes over CdS directionally migrate to the catalytic sites of MoS_2 and CuS, respectively, thus achieving efficient charge separation. In

contrast, the control sample C-C-M, with randomly loaded MoS_2 and CuS onto CdS NWs, lacked the ability for directional carrier migration. The random distribution of MoS_2 and CuS on CdS NWs cannot fully utilize the spatial unidirectional high-efficiency charge transport characteristics of the one-dimensional CdS NWs and is prone to forming electron–hole recombination centers, which are detrimental to carrier separation and migration (Fig. S4b†). Meanwhile, the control sample C/C/M, constructed by *in situ* generation of CuS on the CdS surface through ion exchange and then loading an equivalent amount of MoS_2, also lacks the efficient directional carrier migration capability. As shown in Fig. S4c,† the CuS/CdS P–N heterojunction on the CdS surface blocks the electron transfer pathway from CdS to MoS_2, hindering rapid separation and migration of carriers. Therefore, the photocatalytic activity of the control samples C-C-M and C/C/M is significantly lower than that of CM^2C^1, further confirming the crucial role of selective loading of MoS_2 and CuS on CdS NWs in finely tuning carrier migration and suppressing carrier recombination. As shown in Fig. 3d, the dumbbell-shaped CM^2C^1 heterostructure demonstrates the highest apparent quantum yield (A.Q.Y) at 450 nm, which is consistent with the DRS result, indicating the predominant role of photoexcitation of CdS NWs. Additionally, it was found from Fig. S5† that the photocatalytic hydrogen evolution rate of CM^2C^1 increases with increasing light intensity, confirming that it is indeed a photocatalytic process. Moreover, as shown in Fig. 3e, the photocatalytic activity of the dumbbell-shaped CM^2 binary nanocomposite decreases substantially after the first reaction run, indicating that the MoS_2 clusters at both ends of CdS NWs as charge collectors are conducive to the separation of charge carriers, but the holes accumulating on the sidewalls of CdS NWs oxidize the lattice sulfide ions, leading to photo-corrosion and reduced photoactivity. In contrast, the dumbbell-shaped CM^2C^1 ternary heterostructure still exhibits good photoactivity after four cycles (Fig. 3f), indicating that CuS coating on the sidewalls of CdS NWs for constructing a CdS/CuS P–N heterojunction is beneficial for stabilizing CM^2C^1. Under the driving force of a built-in electric field provided by the P–N heterojunction, hole migration from CdS to CuS is accelerated, which prevents the hole oxidation of the CdS NWs and thus improves the photostability. Furthermore, the good photostability of CM^2C^1 was consistently confirmed by the XRD (Fig. S6†), Raman (Fig. S7†), SEM (Fig. S8†), and XPS (Fig. S9†) results after the cyclic reaction. Additionally, as shown in Table S4,† the photocatalytic activity of the dumbbell-shaped CM^2C^1 reported in our work outperforms previously documented catalysts associated with CdS.

In addition, the photocatalytic activity of the dumbbell-shaped CM^2C^1 heterostructure for the reduction of aromatic nitro compounds was also investigated under visible light. Control experiments were conducted without light exposure and without adding the CM^2C^1 catalyst to verify that the selective reduction of 4-nitroaniline (4-NA) to 4-phenylenediamine (4-PDA) is a photocatalytic reaction (Fig. S10†). Fig. 4a shows the photocatalytic activities of CdS NWs, CM^2 and CM^2C^1 for the photoreduction of 4-NA under visible light irradiation. The low photoreduction activity of pure CdS is related to the rapid recombination of photogenerated charge carriers. It is noteworthy that the photoactivity of CM^2 is significantly enhanced after the selective growth of MoS_2 clusters at both ends of CdS NWs, indicating that the MoS_2 clusters act as electron collectors to promote the directed migration of photogenerated electrons and suppress the recombination of photogenerated charge carriers. Compared with CdS NWs and CM^2, CM^2C^1 demonstrates optimal photocatalytic activity, indicating that the construction of CdS/CuS P–N heterojunctions on the sidewall of CdS NWs promotes the directional migration of holes from CdS to CuS, achieving the spatial separation of electrons and holes and effectively enhancing photocatalytic activity. Meanwhile, CM^2C^1 also exhibits similar optimal photocatalytic activities for the reduction of 3-nitroaniline (3-NA) (Fig. 4b), 2-nitroaniline (2-NA) (Fig. 4c), 4-nitrophenol (4-NP) (Fig. 4d), 3-nitrophenol (3NP) (Fig. 4e), and 2-nitrophenol (2-NP) (Fig. 4f). The photocatalytic performances of C-C-M, C/C/M and CM^2C^1 were also probed under the same conditions (Fig. S11 and S12†). Taking the photoreduction of 4-NA as an example, it was found that the photocatalytic activity of CM^2C^1 is always higher than those of C-C-M (Fig. 4g) and C/C/M (Fig. 4h), further validating the significant role of selectively integrating MoS_2 and CuS on CdS NWs in finely tuning carrier transport and suppressing carrier recombination. As shown in Fig. 4i, without the addition of a hole scavenger, the photocatalytic activity of CM^2C^1 is markedly reduced, confirming the vital role of ammonium formate in quenching holes and inhibiting carrier recombination. Furthermore, the photocatalytic performances of CM^2C^1 with and without adding an electron scavenger were probed ($AgNO_3$) (Fig. S13†). When the electron scavenger $AgNO_3$ was added to the reaction system, CM^2C^1 showed no photocatalytic activity, effectively confirming the crucial role of electrons in stimulating the photoreduction catalysis.

3.3. PEC performances

The photoelectrochemical (PEC) performances of CdS, CM^2 and CM^2C^1 were probed to evaluate the interfacial charge separation efficiency. The transient photocurrent responses of CdS NWs, CM^2, and CM^2C^1 under periodic on-off illumination conditions ($\lambda > 420$ nm) were recorded. As displayed in Fig. 5a, compared with pure CdS NWs, CM^2 exhibits a higher photocurrent density, indicating that selective growth of MoS_2 clusters at both ends of CdS NWs can effectively promote the spatial separation and migration of charge carriers. It is worth noting that CM^2C^1 exhibits a higher photocurrent response compared with CM^2, which indicates that the synergistic effect between the electron-withdrawing capability of MoS_2 clusters and P–N heterojunctions of Cu/CdS plays a significant role in finely tuning carrier migration and suppressing carrier recombination. The electrochemical impedance spectroscopy (EIS) results of CdS NWs, CM^2 and CM^2C^1 are shown in Fig. 5b. Compared with CdS NWs and CM^2, CM^2C^1 demonstrates the smallest arc radius, which confirms that CM^2C^1 shows the lowest carrier transfer resistance, inhibiting the recombination of photogenerated electron–hole pairs. In addition, the charge recombination dynamics of CdS NWs, CM^2 and CM^2C^1 were investigated

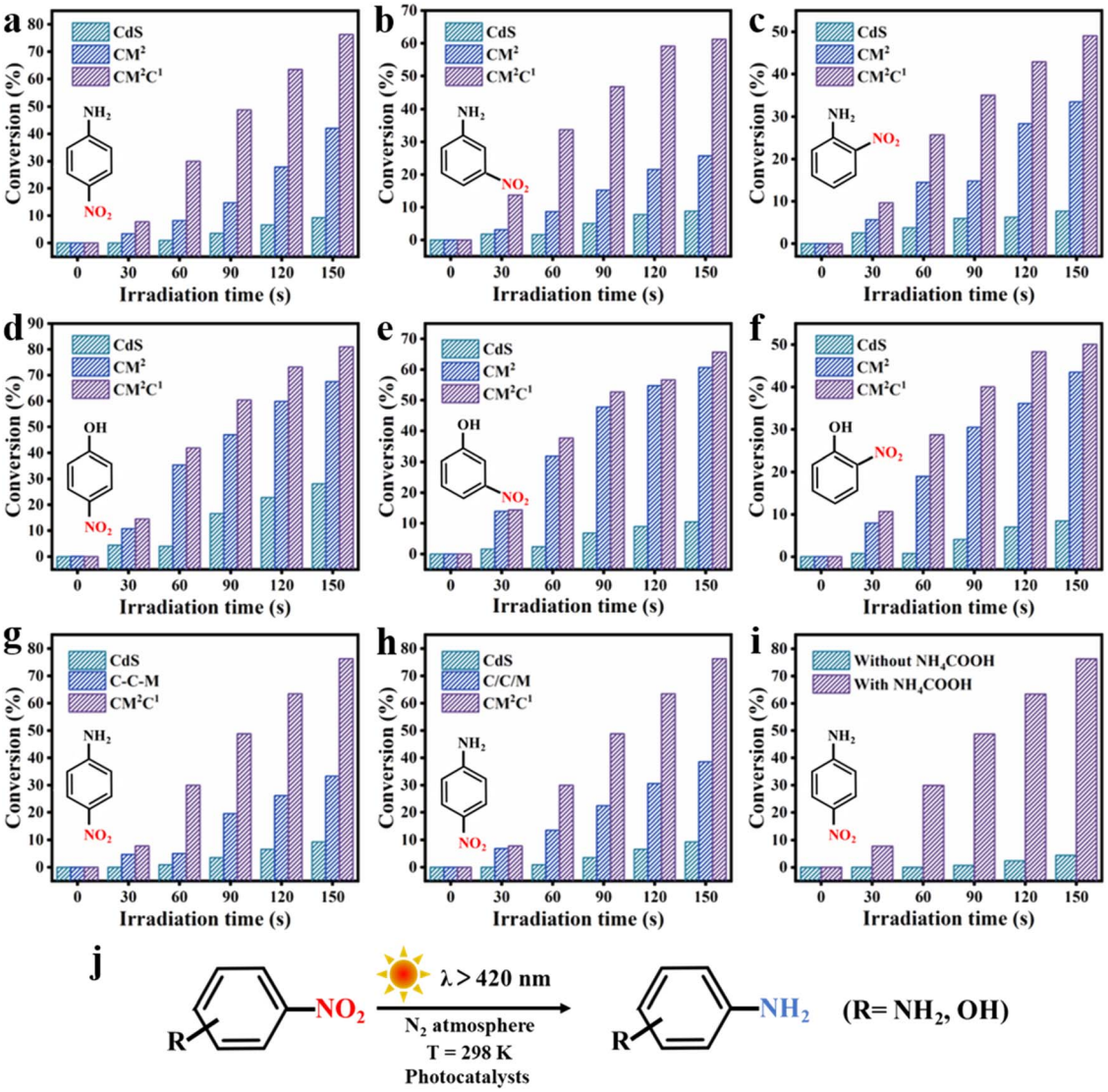

Fig. 4 Photoactivities of CdS, CM^2 and CM^2C^1 for the photoreduction of nitroaromatics including (a) 4-NA, (b) 3-NA, (c) 2-NA, (d) 4-NP, (e) 3-NP, and (f) 2-NP. Photoactivities of CdS, C-C-M, and CM^2C^1 for the photoreduction of (g) 4-NA, photocatalytic activities of CdS, C/C/M and CM^2C^1 for the photoreduction of (h) 4-NA, and photocatalytic performances of CM^2C^1 for the photoreduction of (i) 4-NA with and without adding NH_4COOH. The typical reaction model (j) under the current experimental conditions.

through open circuit voltage decay (OCVD) measurement. As shown in Fig. 5c, CM^2C^1 exhibits the highest photovoltage and longest electron lifetime (Fig. 5d). This suggests that constructing a dumbbell-shaped CM^2C^1 heterostructure by selectively loading MoS_2 and CuS on CdS NWs effectively facilitates the separation and migration of carriers. Besides, charge transfer kinetics were additionally investigated by steady-state photoluminescence spectroscopy (PL) (Fig. 5e), wherein CM^2C^1 shows the lowest PL intensity compared with CdS NWs and CM^2, once again verifying the most efficient charge separation over CM^2C^1.

On the other hand, since the Ksp values of CuS (6.3×10^{-36}) and Ag_2S (6.3×10^{-50})[25] are smaller than that of CdS (8.0×10^{-27}) and both CuS and Ag_2S are p-type semiconductors,[37] they can form a built-in electric field with the n-type semiconductor CdS, thus promoting charge separation. Therefore, a dumbbell-shaped $CdS/MoS_2/Ag_2S$ (CMA) ternary heterostructure photocatalyst was synthesized through a similar method to validate the universal role of the dumbbell-shaped heterostructure in finely tuning carrier transport. As illustrated in Fig. S14,† CMA not only retains the dumbbell-shaped structure but also shows deposition of Ag_2S nanoparticles on the sidewall of CdS NWs. It can be visually observed that MoS_2 and Ag_2S are selectively integrated onto the CdS NWs to construct a ternary dumbbell-shaped CMA heterostructure. By conducting HRTEM tests on ternary CMA composite catalysts, the integration of Ag_2S and MoS_2 on CdS NWs was further analyzed (Fig. S15†). It was observed that distinct MoS_2 clusters appeared at the ends of the CdS NWs. Additionally, lattice stripes of 0.242 and 0.357 nm are identified on the CdS NWs, corresponding to the (013) crystal

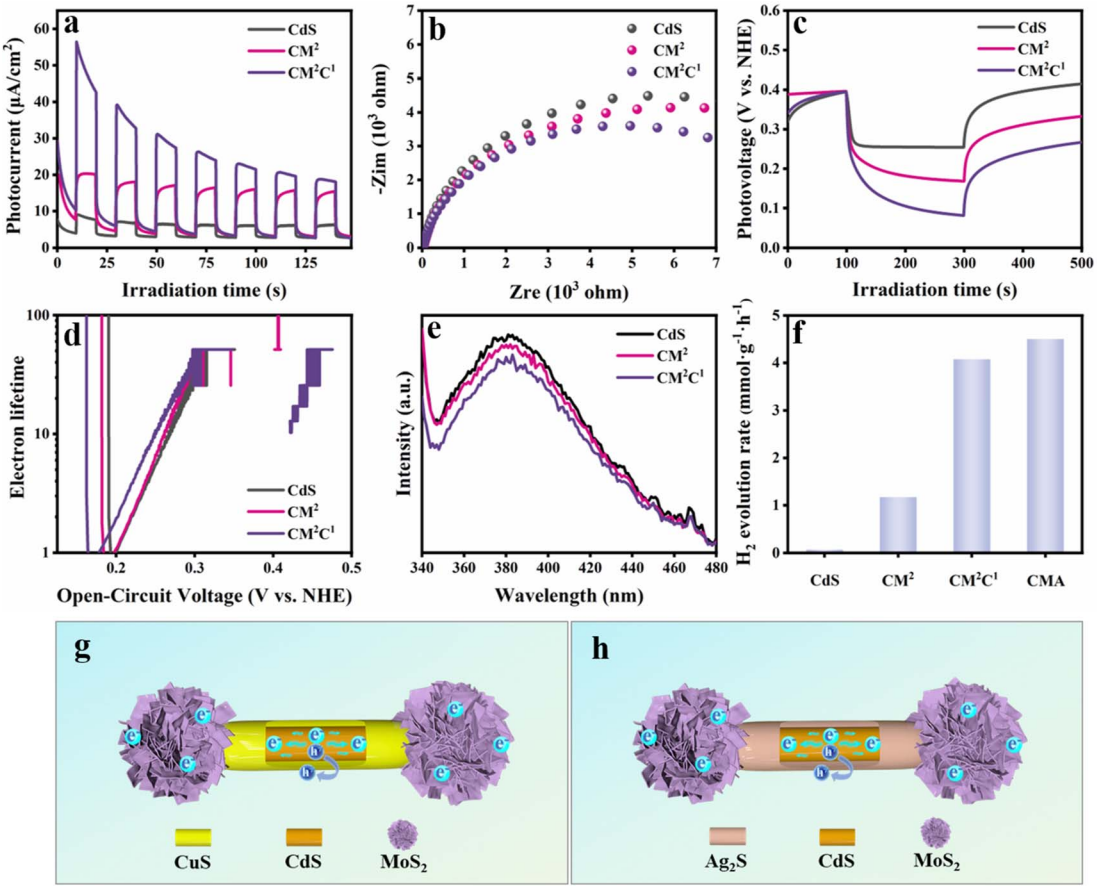

Fig. 5 (a) *I*–*t*, (b) EIS, (c) OCVD and (d) electron lifetime of CdS, CM^2 and CM^2C^1 under visible light (λ > 420 nm) irradiation, (e) PL results of CdS, CM^2 and CM^2C^1, (f) photocatalytic hydrogen evolution performances of CdS, CM^2 and CMA, and schematic diagram of photoelectron transfer over the (g) CdS/MoS_2/CuS and (h) CdS/MoS_2/Ag_2S heterostructure.

plane of Ag_2S and the (100) crystal plane of CdS, respectively. Furthermore, by analyzing the high-resolution Ag 3d spectrum in CMA (Fig. S16c†), it can be found that the peaks at 368.04 (Ag $3d_{5/2}$) and 374.03 (Ag $3d_{3/2}$) eV correspond to the Ag^+ species in Ag_2S, respectively.[38,39] These results confirm the successful integration of Ag_2S and MoS_2 on the CdS NWs to construct a dumbbell-shaped CMA ternary heterostructure. In addition, the charge transfer models of CMC and CMA heterostructures are shown in Fig. 5g and h, respectively. Compared with those of CdS and CM^2, the photocatalytic activities of the CMA and CM^2C^1 ternary dumbbell-shaped heterostructures have been significantly enhanced (Fig. 5f), indicating the synergy of MoS_2 and Ag_2S in promoting the separation and migration of charge carriers. Furthermore, the photocatalytic stability of CMA was verified by cyclic reaction (Fig. S17b†), XRD (Fig. S18†) and Raman (Fig. S19†) results. Similarly, as shown in Fig. S20,† the PEC results of CMA agree well with the photocatalytic activity. Specifically, compared with CdS and CM^2, CMA exhibits optimal photocurrent density and the lowest interfacial charge transfer resistance. This indicates that selective loading of MoS_2 and Ag_2S on the CdS NWs effectively enhances the separation and migration of charge carriers, thereby resulting in enhanced photoactivity. These results further validate the universal role of the dumbbell-shaped heterostructure in finely tuning the dynamics of charge carriers.

3.4. Photocatalytic mechanism

Based on the above results, the photocatalytic mechanism of the dumbbell-shaped CdS/MoS_2/CuS heterostructure was proposed (Scheme 2). The conduction band (CB) and valence band (VB) potentials of CdS and CuS were determined based on the DRS and M–S results. The CB and VB potentials of CdS are determined to be −1.17 and 1.3 eV (*vs.* NHE) (Fig. S21†), respectively, while those of CuS are 0.56 and 1.79 eV (*vs.* NHE) (Fig. S22†), respectively. It is worth noting that the positive M–S slope of CdS indicates that it is a typical n-type semiconductor (Fig. S21a†), whereas the negative M–S slope of CuS indicates that it is a typical p-type semiconductor (Fig. S22a†). The Fermi level of the n-type semiconductor CdS is close to its CB, while the Fermi level of the p-type semiconductor CuS is close to its VB, making the Fermi level of CdS more negative than that of CuS. Due to the difference in Fermi levels, when CdS contacts CuS, the free electrons on CdS migrate towards CuS until they reach the same Fermi level, forming a P–N heterojunction at the contact interface (Fig. S23†). When the CdS/MoS_2/CuS heterostructure is photoexcited by visible light, the built-in electric

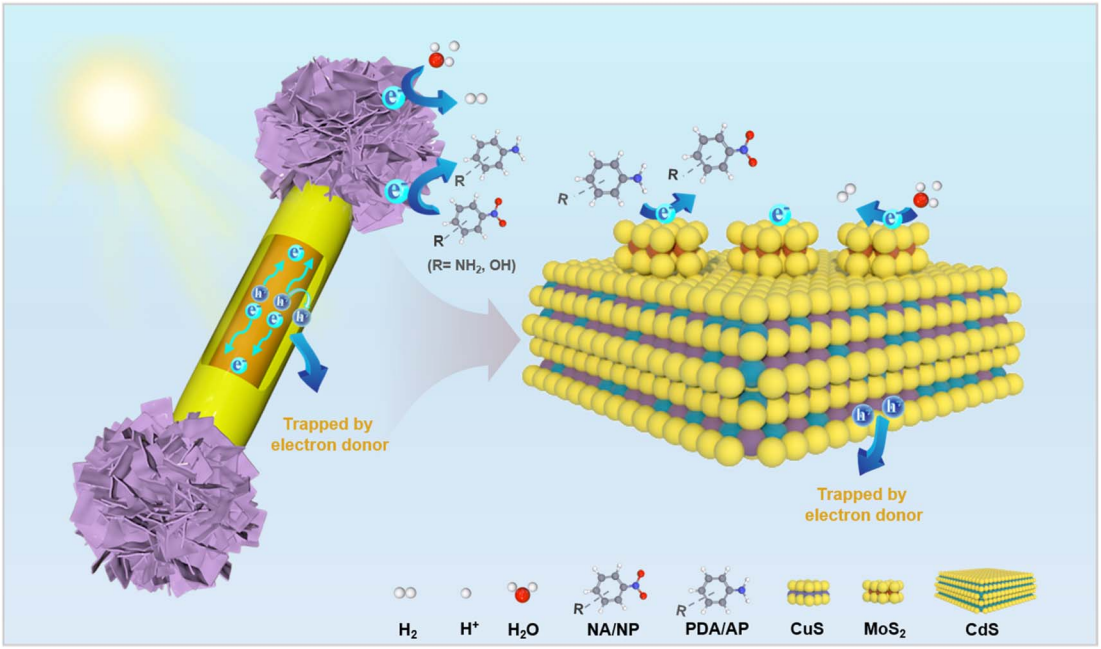

Scheme 2 Schematic illustration of the photocatalytic mechanism of the CdS/MoS_2/CuS heterostructure.

field (electric field direction from CdS to CuS) promotes the migration of CB electrons from CuS to CdS and eventually to MoS_2 clusters for a reduction reaction. Meanwhile, the migration of VB holes from CdS to CuS is stimulated and ultimately quenched by a sacrificial reagent (Fig. S24†). Through this charge transfer pathway, photogenerated electron–hole pairs on CdS are effectively separated, and the electrons on CdS are quickly transferred to MoS_2 clusters to reduce H^+/H_2O to hydrogen, and simultaneously, the holes on CuS are quenched by sacrificial reagents (S^{2-} and SO_3^{2-}). For the photoreduction of aromatic nitro compounds, hole scavengers (ammonium formate) are added to the reaction system to ensure that electrons are the only active species. The electrons trapped by the terminal MoS_2 clusters convert aromatic nitro compounds into amino derivatives, while the VB holes in CuS are completely quenched by the electron donor or hole scavenger. Consequently, the unique integration mode of the dumbbell-shaped CdS/MoS_2/CuS heterostructure effectively promotes the directed migration of photogenerated electrons/holes through the synergistic effect of CuS and MoS_2, significantly improving the photocatalytic performances.

4. Conclusions

In summary, a ternary heterostructure photocatalyst, CdS/MoS_2/CuS, with a distinctive dumbbell-shaped structure was crafted through a simple hydrothermal reaction coupled with a cation exchange strategy. The unique integration mode endows the CdS/MoS_2/CuS heterostructure with abundant reaction active sites, good stability and efficient vectorial carrier transport efficiency. Under the influence of synergy stemming from the unique integration mode between CuS and MoS_2, electrons and holes photoexcited over CdS are rapidly transferred to the electron collector (MoS_2) and hole capture sites (CuS), respectively, to participate in photoredox reactions. These unique structural advantages endow the CdS/MoS_2/CuS ternary heterostructure with significantly enhanced photocatalytic performances for hydrogen evolution and selective reduction of nitroaromatic to amino derivatives under visible light. Our work provides an effective strategy for designing and developing multi-component heterostructures to regulate vectorial charge transfer at the nanoscale.

Data availability

All data supporting the findings of this study are available within the paper and its ESI† files. Source data are provided with this paper.

Author contributions

Peng Su performed the experiments, analyzed all data, and drafted the manuscript. Xian Yan helped review the manuscript. Fang-Xing Xiao guided this work and corrected the manuscript. All the authors contributed to critical discussions on the data and manuscript.

Conflicts of interest

The authors declare no competing interests.

Acknowledgements

The support provided by the Award Program for Minjiang Scholar Professorship is greatly acknowledged. This work was financially supported by the National Natural Science

Foundation of China (no. 21703038 and 22072025). The financial support from the State Key Laboratory of Structural Chemistry, Fujian Institute of Research on the Structure of Matter, Chinese Academy of Sciences is acknowledged (no. 20240018).

References

1 X. Lin, S. Xu, Z. Q. Wei, S. Hou and F. X. Xiao, Selective organic transformation over a self-assembled all-solid-state Z-scheme core–shell photoredox system, *J. Mater. Chem. A*, 2020, **8**, 20151–20161.

2 L. Zhang, X. Jiang, Z. Jin and N. Tsubaki, Spatially Separated Catalytic Sites Supplied with CdS-MoS_2-In_2O_3 Ternary Dumbbell S-scheme heterojunction For Enhanced Photocatalytic Hydrogen Production, *J. Mater. Chem. A*, 2022, **10**, 10715–10728.

3 Y. G. Hu, F. Zhan, Q. Wang, Y. J. Sun, C. Yu, X. Zhao, H. Wang, R. Long, G. Z. Zhang, C. Gao, W. K. Zhang, J. Jiang, Y. Tao and Y. J. Xiong, Tracking Mechanistic Pathway of Photocatalytic CO_2 Reaction at Ni Sites Using Operando, Time-Resolved Spectroscopy, *J. Am. Chem. Soc.*, 2020, **142**, 5618–5626.

4 Q. Zhu, Z. Xu, B. Qiu, M. Xing and J. Zhang, Emerging Cocatalysts on g-C_3N_4 for Photocatalytic Hydrogen Evolution, *Small*, 2021, **17**, 2101070.

5 G. G. Zhang, Z. A. Lan and X. C. Wang, Conjugated Polymers: Catalysts for Photocatalytic Hydrogen Evolution, *Angew. Chem., Int. Ed.*, 2016, **55**, 15712–15727.

6 X. Yan, J. H. Dong, J. Y. Zheng, Y. Wu and F. X. Xiao, Customizing precise, tunable, and universal cascade charge transfer chains towards versatile photoredox catalysis, *Chem. Sci.*, 2024, **15**, 2898–2913.

7 X. Yan, M. Yuan, Y. L. Yuan, P. Su, Q. Chen and F. X. Xiao, Photocarrier tunneling triggering CO_2 photocatalysis, *Chem. Sci.*, 2024, **15**, 10625–10637.

8 P. Rong, Y. F. Jiang, Q. Wang, M. Gu, X. L. Jiang and Q. Yu, Photocatalytic degradation of methylene blue (MB) with Cu1-ZnO single atom catalysts on graphene-coated flexible substrates, *J. Mater. Chem. A*, 2022, **10**, 6231–6241.

9 V. Polliotto, S. Livraghi, A. Krukowska, M. V. Dozzi, A. Zaleska-Medynska, E. Selli and E. Giamello, Copper-Modified TiO_2 and $ZrTiO_4$: Cu Oxidation State Evolution during Photocatalytic Hydrogen Production, *ACS Appl. Mater. Interfaces*, 2018, **10**, 27745–27756.

10 W. Yang, M. Xu, K. Y. Tao, J. H. Zhang, D. C. Zhong and T. B. Lu, Building 2D/2D CdS/MOLs Heterojunctions for Efficient Photocatalytic Hydrogen Evolution, *Small*, 2022, **18**, 2200332.

11 S. Q. Luo, H. W. Lin, Q. Wang, X. H. Ren, D. Hernández-Pinilla, T. Nagao, Y. Xie, G. L. Yang, S. J. Li, H. Song, M. Oshikiri and J. H. Ye, Triggering Water and Methanol Activation for Solar-Driven H_2 Production: Interplay of Dual Active Sites over Plasmonic ZnCu Alloy, *J. Am. Chem. Soc.*, 2021, **143**, 12145–12153.

12 F. X. Xiao, J. W. Miao, H. Y. Wang and B. Liu, Self-assembly of hierarchically ordered CdS quantum dots-TiO_2 nanotube array heterostructures as efficient visible light photocatalysts for photoredox applications, *J. Mater. Chem. A*, 2013, **1**, 12229–12238.

13 X. F. Gao, H. B. Li, W. T. Sun, Q. Chen, F. Q. Tang and L. M. Peng, CdTe Quantum Dots-Sensitized TiO_2 Nanotube Array Photoelectrodes, *J. Phys. Chem. C*, 2009, **113**, 7531–7535.

14 S. R. Xu, J. L. Li, Q. L. Mo, K. Wang, G. Wu, Y. Xiao, X. Z. Ge and F. X. Xiao, Steering Photocatalytic CO_2 Conversion over $CsPbBr_3$ Perovskite Nanocrystals by Coupling with Transition-Metal Chalcogenides, *Inorg. Chem.*, 2022, **61**, 17828–17837.

15 R. J. Feng, K. W. Wan, X. Y. Sui, N. Zhao, H. X. Li, W. Y. Lei, J. G. Yu, X. F. Liu, X. H. Shi, M. L. Zhai, G. Liu, H. Wang, L. R. Zheng and M. H. Liu, Anchoring single Pt atoms and black phosphorene dual co-catalysts on CdS nanospheres to boost visible-light photocatalytic H_2 evolution, *Nano Today*, 2021, **37**, 101080.

16 G. W. Wang, G. K. Zhang, X. X. Ke, X. Y. Chen, X. Chen, Y. S. Wang, G. Y. Huang, J. C. Dong, S. Q. Chu and M. L. Sui, Direct Synthesis of Stable 1T-MoS_2 Doped with Ni Single Atoms for Water Splitting in Alkaline Media, *Small*, 2022, **18**, 2107238.

17 K. N. Li, S. S. Zhang, Y. H. Li, J. J. Fan and K. L. Lv, MXenes as noble-metal-alternative co-catalysts in photocatalysis, *Chin. J. Catal.*, 2021, **42**, 3–14.

18 K. L. He, E. Campbell, Z. M. Huang, R. C. Shen, Q. Li, S. Q. Zhang, Y. L. Zhong, P. Zhang and X. Li, Metal Carbide-Based Cocatalysts for Photocatalytic Solar-to-Fuel Conversion, *Small Struct.*, 2022, **3**, 2200104.

19 D. Ding, Z. Jiang, D. Ji, N. V. Myung and L. Zan, Bi_2O_2Se as a novel co-catalyst for photocatalytic hydrogen evolution reaction, *Chem. Eng. J.*, 2020, **400**, 125931.

20 J. Zander and R. Marschall, Ni_2FeS_4 as a highly efficient earth-abundant co-catalyst in photocatalytic hydrogen evolution, *J. Mater. Chem. A*, 2023, **11**, 17066–17078.

21 J. Xiong, J. Di and H. Li, Interface engineering in low-dimensional bismuth-based materials for photoreduction reactions, *J. Mater. Chem. A*, 2021, **9**, 2662–2677.

22 H. Li, Q. Song, S. Wan, C. W. Tung, C. Liu, Y. Pan, G. Luo, H. M. Chen, S. Cao, J. Yu and L. Zhang, Atomic Interface Engineering of Singl-Atom Pt/TiO_2-Ti_3C_2 for Boosting Photocatalytic CO_2 Reduction, *Small*, 2023, **19**, 2301711.

23 X. Hao, Y. Fan, W. Deng and Z. Jin, *In situ* XPS demonstrated efficient charge transfer of ohmic junctions based on graphdiyne (g-C_nH_{2n-2}) nanosheets coupled with porous nanoflowers Ni_5P_4 for efficient photocatalytic H_2 evolution, *Carbon*, 2024, **218**, 118752.

24 Q. Zhao, Z. Tang, Y. Pan, J. Han, J. Yang, Y. Guo, X. Lai, Z. Yang and G. Li, The Ksp gap enabled precipitation transformation reactions from transition metal hydroxides to sulfides for alkali metal ion storage, *Inorg. Chem. Front.*, 2023, **10**, 3406–3414.

25 C. Lu, S. Du, Y. Zhao, Q. Wang, K. Ren, C. Li and W. Dou, Efficient visible-light photocatalytic H_2 evolution with heterostructured Ag_2S modified CdS nanowires, *RSC Adv.*, 2021, **11**, 28211–28222.

26 K. Wang, X. Z. Ge, Q. L. Mo, X. Yan, Y. Xiao, G. Wu, S. R. Xu, J. L. Li, Z. X. Chen and F. X. Xiao, Steering bi-directional charge transfer *via* non-conjugated insulating polymer, *J. Catal.*, 2022, **416**, 92–102.

27 L. F. Luo, Y. D. Wang, S. P. Huo, P. Lv, J. Fang, Y. Yang and B. Fei, Cu-MOF assisted synthesis of CuS/CdS(H)/CdS(C): Enhanced photocatalytic hydrogen production under visible light, *Int. J. Hydrogen Energy*, 2019, **44**, 30965–30973.

28 C. Lai, M. M. Zhang, B. S. Li, D. L. Huang, G. M. Zeng, L. Qin, X. G. Liu, H. Yi, M. Cheng, L. Li, Z. Chen and L. Chen, Fabrication of CuS/$BiVO_4$ (040) binary heterojunction photocatalysts with enhanced photocatalytic activity for Ciprofloxacin degradation and mechanism insight, *Chem. Eng. J.*, 2019, **358**, 891–902.

29 B. Qiu, L. Cai, N. Zhang, X. Tao and Y. Chai, A Ternary Dumbbell Structure with Spatially Separated Catalytic Sites for Photocatalytic Overall Water Splitting, *Adv. Sci.*, 2020, **7**, 1903568.

30 X. X. Lu, W. J. Chen, Y. Yao, X. M. Wen, J. N. Hart, C. Tsounis, C. Y. Toe, J. Scott and Y. H. Ng, Photogenerated charge dynamics of CdS nanorods with spatially distributed MoS_2 for photocatalytic hydrogen generation, *Chem. Eng. J.*, 2021, **420**, 127709.

31 X. Y. Fu, Y. B. Li, M. H. Huang, T. Li, X. C. Dai, S. Hou, Z. Q. Wei and F. X. Xiao, Partially Self-Transformed Transition-Metal Chalcogenide Interim Layer: Motivating Charge Transport Cascade for Solar Hydrogen Evolution, *Inorg. Chem.*, 2020, **59**, 2562–2574.

32 Y. Li, Q. Zhao, Y. Zhang, Y. Li, L. Fan, F.-t. Li and X. Li, In-situ construction of sequential heterostructured CoS/CdS/CuS for building "electron-welcome zone" to enhance solar-to-hydrogen conversion, *Appl. Catal., B*, 2022, **300**, 120763.

33 Y. L. Han, X. F. Dong and Z. B. Siang, Synthesis of $Mn_xCd_{1-x}S$ nanorods and modification with CuS for extraordinarily superior photocatalytic H_2 production, *Catal. Sci. Technol.*, 2019, **9**, 1427–1436.

34 G. Eda, H. Yamaguchi, D. Voiry, T. Fujita, M. W. Chen and M. Chhowalla, Photoluminescence from Chemically Exfoliated MoS_2, *Nano Lett.*, 2011, **11**, 5111–5116.

35 S. Huang, C. Chen, H. Tsai, J. Shaya and C. Lu, Photocatalytic degradation of thiobencarb by a visible light-driven MoS_2 photocatalyst, *Sep. Purif. Technol.*, 2018, **197**, 147–155.

36 R. Gusain, N. Kumar, F. Opoku, P. P. Govender and S. S. Ray, MoS_2 Nanosheet/ZnS Composites for the Visible-Light-Assisted Photocatalytic Degradation of Oxytetracycline, *ACS Appl. Nano Mater.*, 2021, **4**, 4721–4734.

37 W. Zhao, B. Dai, F. Zhu, X. Tu, J. Xu, L. Zhang, S. Li, D. Y. C. Leung and C. Sun, A novel 3D plasmonic p–n heterojunction photocatalyst: Ag nanoparticles on flower-like p-Ag_2S/n-$BiVO_4$ and its excellent photocatalytic reduction and oxidation activities, *Appl. Catal., B*, 2018, **229**, 171–180.

38 L. Deng, D. Yin, K. K. Khaing, S. Xiao, L. Li, X. Guo, J. Wang and Y. Zhang, The facile boosting sunlight-driven photocatalytic performance of a metal–organic-framework through coupling with Ag_2S nanoparticles, *New J. Chem.*, 2020, **44**, 12568–12578.

39 C. Chen, Z. Li, H. Lin, G. Wang, J. Liao, M. Li, S. Lv and W. Li, Enhanced visible light photocatalytic performance of ZnO nanowires integrated with CdS and Ag_2S, *Dalton Trans.*, 2016, **45**, 3750–3758.